Atg11 promotes Kar9-mediated alignment of the mitotic spindle

Md. Hashim Reza[1], Jigyasa Verma[1$], Ratul Chowdhury[2], Ravi Manjithaya[3], and Kaustuv Sanyal[1, 4*]

[1]Molecular Mycology Laboratory, Molecular Biology and Genetics Unit, Jawaharlal Nehru Centre for Advanced Scientific Research, Jakkur, Bangalore 560 064, India.

[2]Department of Systems Biology, Harvard Medical School, Boston, MA 02115, USA.

[3]Autophagy Laboratory, Molecular Biology and Genetics Unit, Jawaharlal Nehru Centre for Advanced Scientific Research, Jakkur, Bangalore 560 064, India.

[4]Osaka University, Suita, Osaka 565 0871, Japan.

*Corresponding author: Molecular Mycology Laboratory, Molecular Biology and Genetics Unit, Jawaharlal Nehru Centre for Advanced Scientific Research, Jakkur, Bangalore 560 064, India. Phone: +91 80 2208 2878, e-mail: sanyal@jncasr.ac.in

[$]Present address: Department of Cellular and Physiological Sciences, University of British Columbia, Vancouver, BC, V6T1Z3, Canada.

Keywords: autophagy, chromosome segregation, kinetochore, SPB asymmetry, spindle position checkpoint, motor proteins

Abstract

Asymmetric spindle pole body (SPB) inheritance requires a cascade of events that involve kinases, phosphatases and structural scaffold proteins including molecular motors and microtubule-associated proteins. Higher levels of an SPB component Spc72 and the spindle positioning factor Kar9 at the old SPB, which migrates to the daughter cell, ensure asymmetric SPB inheritance. In this study, by analyzing the protein interaction network of autophagy (Atg)-related proteins with those that constitute the chromosome segregation machinery, and growth inhibition kinetics in the presence of a microtubule poison, we identified Atg11 as a potential regulator of chromosome transmission from a cohort of 35 autophagy mutants in *Saccharomyces cerevisiae*. Cells lacking Atg11 did not show kinetochore defects but displayed a high rate of chromosome loss and delayed anaphase onset. Atg11 positively interacted with Kar9 and Kip2 and negatively with Dyn1 and Kar3 in mediating proper positioning and alignment of the mitotic spindle that was found to be under the surveillance of the spindle positioning checkpoint. Indeed, *atg11*Δ cells displayed an inverted SPB inheritance. Our experiments further revealed that via the Kar9 pathway, Atg11 promotes asymmetric localization of Spc72 and Kar9 on the old SPB. Atg11 physically interacted with Spc72 and transiently localized close to the old SPB during metaphase-to-anaphase progression. Thus, we uncover an autophagy-independent role of Atg11 in spindle alignment. This study emphasizes the importance of screens to identify factors mediating the complex and intricate crosstalk between biological processes fundamental to genomic integrity.

Introduction

Saccharomyces cerevisiae divides asymmetrically producing daughter cells that are distinct from the mother in size, the molecular composition of proteins and organelles, and replicative lifespan (RLS). The alignment of the mitotic spindle along the predetermined polarity axis is critical for proper nuclear division during asymmetric cell division. In budding yeast, the spatial crosstalk between astral microtubules (aMTs) and cortical cues regulating mitotic spindle alignment along the polarity axis requires the action of two functionally redundant MT-associated pathways. At metaphase, Kar9 mediates the mitotic spindle alignment along the polarity axis at the bud-neck, where it interacts with the plus-end tracking protein Bim1 at one end (Korinek et al., 2000, Lee et al., 2000, Miller et al., 2000), and Myo2, a type V myosin, on the other (Yin et al., 2000). The dynein-dependent pathway operates at anaphase and generates pulling forces to orient the nucleus along the polarity axis (Segal and Bloom, 2001, Yeh et al., 1995). Mutations in proteins altering the function of either of these two pathways often misalign the spindle (Li et al., 1993, Matellan et al., 2020, Miller and Rose, 1998, Soues and Adams, 1998). While one pathway compensates for the other, loss of both is lethal for the cell (Miller and Rose, 1998). Misaligned spindles lead to the activation of spindle position checkpoint (SPOC) (Bloecher et al., 2000, Nelson et al., 2012, Pereira et al., 2000, Wang et al., 2000, Yeh et al., 1995), a surveillance mechanism that halts the cell cycle and prevents the exit from mitosis by inhibiting the mitotic exit network (MEN) signalling.

MT dynamics and spindle positioning are also regulated by cytoplasmic motor dynein and kinesin-related proteins (KRPs) which facilitate equal nuclear segregation in two daughter cells. Kip3 belongs to the kinesin-8/kinesin-13 family and causes MT depolymerization at the more dynamic plus ends of MTs (Niederstrasser et al., 2002). Kip2, a plus-end directed motor, localizes to the spindle pole bodies (SPBs) and has been shown to play a role in the polymerization of cytoplasmic MTs (Cottingham and Hoyt, 1997). In contrast, Kar3, belonging to the kinesin-14 family, is a minus end-directed motor and primarily acts at SPBs, where it depolymerizes both cytoplasmic and nuclear MTs and regulates the spindle length dynamics at metaphase (Huyett et al., 1998).

MTs emanate from MT-organizing centers (MTOCs), which are centrosomes in metazoans and SPBs in budding yeast. Each SPB nucleates nuclear and aMTs from its nuclear and cytosolic faces, respectively. MT nucleation is facilitated by the recruitment of the conserved γ-tubulin complex (γTC), composed of Tub4, Spc97 and Spc98 (Farache et al., 2018, Geissler et al., 1996, Knop et al., 1997, Kollman et al., 2011, Winey and Bloom, 2012), onto Spc110 at the inner plaque (Knop and Schiebel, 1997) and Spc72 at the outer plaque or Kar1

at the half-bridge (Gruneberg et al., 2000, Knop and Schiebel, 1998, Lin et al., 2015, Pereira et al., 1999). Immediately after SPB duplication, kinases and phosphatases contribute to the establishment and maintenance of SPB asymmetry through a cascade of events, leading to a difference in protein composition, age, and structure between the two SPBs. During the cell cycle, the pre-existing old SPB migrates to the daughter cell while and the newly formed SPB remains in the mother. Cdc5, a polo-like kinase, localizes to the SPBs and contributes to the timely and sequential recruitment of Spc72 and Kar9, the two major determinants of SPB inheritance (Matellan et al., 2020).

Two different premises suggest aMT asymmetry stems from the contribution of extrinsic and intrinsic factors. The cyclin-dependent kinase (CDK) Cdc28/Cdk1 facilitates the biased recruitment of Spc72 and the γTC at the old SPB during the early cell cycle stage, and subsequently promotes the assembly of the new SPB in the correct order with the recruitment of the outer plaque following complete assembly of the inner plaque (Geymonat et al., 2020). This intrinsic asymmetry of SPB core proteins contributes to aMT asymmetry and spindle polarity in dividing cells. On the other hand, the microtubule plus-end tracking protein (+TIP) Kar9 represents the extrinsic control of aMT asymmetry (Lengefeld and Barral, 2018). Kar9, being present at both the poles during the onset of SPB separation, gets phosphorylated at the new SPB by Cdk1/Clb4 during cell cycle progression and thus displays asymmetric localization at the old SPB, enabling spindle alignment along the polarity axis (Meziane et al., 2021). Any perturbations in spindle alignment and consequently in the asymmetric cell division has wide implications ranging from early ageing with a decreased RLS, aneuploidy and cancer, to a failure in embryonic development. Therefore, it is imperative to identify new players contributing to the spindle positioning.

With multiple reports of genetic and/or physical interactions between autophagy and chromosome segregation machinery proteins, the motivation of the present study was to investigate the role of autophagy protein(s) in mediating faithful chromosome segregation in the budding yeast, *S. cerevisiae*, which undergoes closed mitosis. Autophagy is a catabolic process of degradation of misfolded proteins and damaged organelles and is predominantly a cytoplasmic process. Under stress and starvation conditions, autophagy is induced and involves Atg17-meditated non-selective degradation of cargoes, while Atg11 mediates selective autophagy predominantly under vegetative conditions (Matscheko et al., 2019). Recent studies highlight the role of autophagy in cell metabolism, growth, ageing, and genome stability (Dotiwala et al., 2013, Matsui et al., 2013b, Vessoni et al., 2013). Here, by using a phenotypic screen we identified Atg11, from a collection of autophagy mutants, as a regulator of high-

fidelity chromosome segregation. Our results uncover a previously unknown autophagy-independent function of Atg11 in mediating asymmetric SPB segregation to help proper spindle alignment during mitosis.

Results

Atg11 plays an autophagy-independent role in high-fidelity chromosome transmission

We collated all reported interactions of autophagy proteins with proteins involved in the chromosome segregation machinery using Perl scripts to query the latest curation of the BioGRID yeast interactomes (Stark et al., 2006) (Figure S1A). Atg11 displayed interactions with Spc72 and Bud2 which play a critical role in mitotic spindle alignment and spindle positioning checkpoint respectively (Figure 1A). This prompted us to carry out a phenotypic screen to determine growth kinetics of *atg* null mutants to microtubule depolymerizing drug, thiabendazole (TBZ). Among the mutants (Figure S2A), *atg11*Δ cells displayed maximum sensitivity to TBZ (Figure 1B), supporting an earlier observation (Strome et al., 2008). An *ATG11*-addback strain complemented the TBZ-induced growth defects in *atg11*Δ cells confirming its specific role in regulating spindle dynamics (Figure 1B). This was further corroborated by the slow growth of *atg11*Δ cells at 37°C (Figure 1C).

Any defects in spindle dynamics negatively impact the fidelity of chromosome segregation. Indeed, a strain harbouring an extra linear chromosome displayed a significantly higher rate of chromosome loss in *atg11*Δ cells at 30°C that further worsened at 37°C (Figure 1D). Similarly, the average mitotic stability of a monocentric circular plasmid was found to be significantly lower in *atg11*Δ cells than in the wild-type but comparable to that of a kinetochore mutant (Figure 1E). No other *atg* mutants tested displayed any drop in the mitotic plasmid stability. Mutants of key autophagy proteins such as *atg1*Δ or *atg17*Δ, required for autophagy during starvation, neither displayed any TBZ sensitivity nor any drop in plasmid stability (Figure 1E). Hence, we conclude that the role of Atg11 in mediating error-free chromosome segregation is independent of its autophagy function.

Atg11 is essential for timely anaphase onset

Flow cytometric analysis revealed an increased population of *atg11*Δ cells at the G2/M stage with 2N DNA content at 30°C that further exacerbated at 37°C (Figure S3A). The increased percentage of large-budded cells at G/M with an unsegregated nucleus indicates the inability of *atg11*Δ cells to segregate chromosomes during mitosis (Figure 2A). The *CEN* transcriptional read-through assay suggested that Atg11 does not play any role in the

maintenance of the kinetochore ensemble (Figure S3B-C). Microscopic examination of Tub1-tagged microtubules revealed the proportion of large-budded cells of *atg11*Δ with short, early anaphase spindle (2-4 µm) was two-fold higher compared to the wild-type that was further increased at a higher temperature (Figure 2B-C). Live-cell imaging using an *atg11*Δ strain carrying marked SPBs (Spc42-mCherry) and the mitotic spindle (GFP-Tub1) confirmed a significant delay in anaphase onset (Figure 2D-E), which resulted in the longer cell cycle in the mutant (Figure 2F-G). This delay is also observed at a higher temperature (Figure S4A-B). Collectively, these results confirm the role of Atg11 in anaphase spindle elongation.

Next, we sought to examine whether the *atg11*Δ-associated spindle defects are under the surveillance of the spindle assembly checkpoint (SAC) and/or spindle positioning checkpoint (SPOC). While SAC is activated in the presence of Mad2, activation of SPOC requires Bub2. Cells of *atg11*Δ *mad2*Δ double mutant were conditionally synthetic lethal in the presence of TBZ or under conditions that compromised spindle dynamics (Figure S5A). The *atg11*Δ *bub2*Δ double mutant, on the other hand, did not show any significant difference in growth at a higher temperature when compared with the *bub2*Δ cells (Figure S5B). Importantly, *atg11*Δ *bub2*Δ double mutant cells but not *atg11*Δ *mad2*Δ cells, displayed a significant bypass of the G2/M arrest, yielding the cell cycle profile similar to that of the wild-type and *bub2*Δ mutant both at 30°C and 37°C (Figure S5C-D). Taken together, these results strongly indicate a SPOC-mediated delay in anaphase onset in the *atg11*Δ cells.

Atg11 helps in spindle alignment by interacting with molecular motors, microtubule-associated proteins (MAPs) and microtubule plus-end tracking proteins (+ TIPs)

Having established the role of Atg11 in spindle elongation, subsequently, we examined its genetic interactions with known regulators of this process. Double mutant cells of *atg11*Δ *kar3*Δ, *atg11*Δ *cik1*Δ, and *atg11*Δ *dyn1*Δ displayed enhanced growth defects at the elevated temperature in the presence or absence of TBZ when compared to their respective null mutants (Figure 3A, Figure S6A-B). A significantly increased proportion of large-budded cells was found to have shorter spindles (2-4 µm) in the *atg11*Δ *kar3*Δ double mutant compared to the *kar3*Δ mutant at 37°C (Figure S6C). On the other hand, double mutant cells of *atg11*Δ *kip2*Δ, *atg11*Δ *bim1*Δ and *atg11*Δ *kar9*Δ grew better than their respective null mutants in presence of TBZ (Figure 3A, Figure S6B). We also observed an increased percentage of cells having the late anaphase spindle in the *atg11*Δ *kip2*Δ double mutant treated with TBZ in comparison to the *kip2*Δ mutant (Figure S6D). Thus, Atg11 displayed positive genetic interactions with a plus-end directed motor or +TIPs while it negatively interacted with minus-end directed

motors. Based on these results, we conclude that in collaboration with cytosolic motors and MAPs, Atg11 plays a role in mediating correct spindle positioning (Figure 3B).

Next, to gain deeper insights, we attempted to determine whether Atg11 influences the Kar9- or dynein-dependent pathway of spindle positioning by examining the effect of low temperature, known to enhance the binucleated phenotype (Yeh et al., 1995). The *dyn1*Δ, *kip2*Δ, and *dyn1*Δ *kip2*Δ double mutant strains exhibited a significant increase in the proportion of binucleated cells as expected (Cottingham and Hoyt, 1997). The *atg11*Δ cells did show a marginal spindle positioning defect (Figure 3C). Remarkably, the *atg11*Δ *dyn1*Δ double mutant not only had a significantly increased proportion of binucleated cells but also displayed mitotic exit with mispositioned spindles, marked by the accumulation of multinucleated and anucleated cells (Figure 3C, Figure S7A). Cells of *kar9*Δ, as well as *atg11*Δ *kar9*Δ, had a higher number of binucleated cells as compared to wild-type (Figure 3C). However, the proportion of binucleated cells in *kar9*Δ was similar to that of *atg11*Δ *kar9*, suggesting that Atg11 contributes to spindle positioning in the Kar9-dependent manner.

Atg11 maintains the asymmetrical distribution of Spc72 to ensure proper SPB inheritance

Having established the participation of Atg11 in the Kar9-dependent spindle positioning, we sought to address whether loss of *ATG11* leads to any perturbation in the alignment of the metaphase spindle and its migration close to the bud-neck. *kar9*Δ cells are known to have defects such as a higher angle of spindle alignment (Liakopoulos et al., 2003) as well as a mispositioned spindle (Hotz et al., 2012). Our analysis suggested that the *atg11*Δ cells had a significantly higher angle of alignment of the spindle than the wild-type (Figure S8A). Cells of *atg11*Δ *kar9*Δ double mutant also showed a higher angle of alignment (Figure S8A). In addition, *atg11*Δ cells displayed a significantly lower percentage of cells having the metaphase spindle at the bud-neck that further exacerbated in the *kar9*Δ mutant cells (Figure S8B). We observed that *atg11*Δ *kar9*Δ double mutant had a significant increase in the proportion of cells having the metaphase spindle at the neck region compared to the *kar9*Δ cells (Figure S8B). Importantly, our analysis of the mispositioned mid-anaphase spindle (4-7 µm) in these mutants did not show any difference between wild-type and *atg11*Δ cells, which suggested that Atg11 does not contribute to anaphase spindle positioning (Figure S8C). Collectively, these results confirm the participation of Atg11 in the Kar9-dependent metaphase spindle positioning.

The Kar9 pathway also specifies SPB inheritance by orienting the old SPB towards the daughter cell (Pereira et al., 2001). The *atg11*Δ cells displayed a two-fold increase in SPB inheritance defects, while *kar9*Δ cells showed approximately a three-fold increase relative to the wild-type (Figure 4A). The *atg11*Δ *kar9*Δ double mutant displayed *kar9*Δ-like SPB inheritance defect (Figure 4A). Notably, the *atg1*Δ mutant, defective in autophagy, segregated the SPBs similar to the wild-type, further confirming that the function of Atg11 in the Kar9-mediated pathway of SPB inheritance is autophagy-independent (Figure 4A).

A previous report on the localization interdependency of Spc72, the γ-tubulin complex receptor, and Kar9 onto the SPBs, established Spc72 acting upstream of Kar9 (Juanes et al., 2013), and that the lack of Spc72 severely affected Kar9 loading on the SPBs (Matellan et al., 2020). We determined that the lack of Atg11 randomized the loading of Spc72 and Kar9 on SPBs (Figure 4B-D), as *atg11*Δ cells displayed a significantly increased proportion of cells having the opposite localization pattern of Spc72 and Kar9 on SPBs (Figure 4C). Strikingly, the loss of *ATG11* impacted the localization of Spc72 onto the old SPB even when Kar9 was correctly localized (Figure 4D). Taken together, these results strongly indicate that Atg11 facilitates the asymmetric localization of Spc72 and Kar9 on the old SPB necessary for the non-random SPB inheritance in budding yeast.

Atg11 is transiently localized to spindle pole bodies

Using a strain that expressed sfGFP-Atg11, we confirmed the canonical localization of the fusion protein onto the vacuolar membrane as a punctate signal at all stages of the cell cycle (Figure S8D). Live-cell imaging of sfGFP-Atg11 and Spc42 (SPBs) in the early anaphase stage revealed proximal localization of Atg11 with the old SPB in a high proportion of the cells (Figure 4E). The Atg11 punctum then migrated to the daughter cell and at a later stage appeared near the new SPB as well (Figure 4E and Figure S8E).

A previous report indicated Atg11 interacts with the SPB protein Spc72 (Wang et al., 2012). Having observed transient SPB localization of Atg11, we performed the yeast two-hybrid (Y2H) assay that confirmed positive interactions between Atg11 and Spc72 (Figure 4F). The Y2H assay with Cnm67, a protein of the outer plaque of the SPB, did not show any interactions with Atg11 (Figure S8F), suggesting that the spatial position of Atg11 and Spc72 is critical for their physical interactions. We also carried out a flexible protein-protein docking study of Atg11 and Spc72 to identify the possible residues necessary for the Atg11-Spc72 interaction using a ClusPro-type algorithm (Kozakov et al., 2017) within the OptMAVEn-2.0 docking protocol (Chowdhury et al., 2018). Analysis of the Spc72 pose, as bound to Atg11,

revealed hydrophobic packing of the peptide termini by Leu868 and Leu1004 residues of Atg11, and electrostatic stabilization of the phosphate group using the positively charged side chain of Asp1001 of Atg11 (Figure S8G). Taken together, these results suggest a transient in vivo localization of Atg11 at the SPBs probably through its association with Spc72.

Discussion

In this study, we took advantage of the reported protein interaction network and identified possible crosstalk between autophagy proteins and those required for chromosome stability in the budding yeast *S. cerevisiae*. This analysis hinted that Atg11 may be involved in the positioning of the mitotic spindle. A parallel unbiased screen using an array of 35 *atg* mutants revealed a significant level of growth inhibition of *atg11*Δ cells in the presence of sublethal concentrations of a microtubule poison. In addition, *atg11*Δ cells, but not other autophagy mutants that were autophagy-deficient, exhibited a high rate of chromosome loss, suggesting that the Atg11's role in chromosome segregation is autophagy-independent.

The molecular mechanism underpinning the role of Atg11 in genome stability remained unknown when the cells are grown in nutrient-rich conditions. First, we determined that the kinetochore integrity in the absence of Atg11 remained intact. Further analysis suggested that Atg11 is required during mitotic progression, as mutant cells accumulated at the early anaphase stage with misaligned spindle under stress conditions that did not affect wild-type cells. As expected, the cell cycle delay was mediated by the spindle positioning checkpoint rather than the spindle assembly checkpoint. Atg11 genetically interacted with cytosolic regulators of spindle positioning including Kar9 that plays a key role in the metaphase spindle alignment. Indeed, Atg11 contributes to the Kar9-dependent pathway of spindle positioning that operates at early anaphase rather than the dynein-mediated late anaphase pathway. To understand the mechanism by which Atg11 participates in spindle positioning, we studied any perturbation of biased asymmetric localization patterns of Spc72 and Kar9 in old (present in the daughter cell) and new (present in the mother cell) SPBs required for directional spindle alignment and elongation. We demonstrated that the loss of function of Atg11 led to inverted SPB asymmetry, due to atypical localization of Spc72 and Kar9. Taking this critical lead forward, we identified physical interactions between Atg11 with Spc72 by Y2H assays as well as transient but distinct cell cycle stage-specific localization of Atg11 proximal to the old SPB. Thus, based on the series of *in silico*, genetic, biochemical and cell biology-based evidence, in this study, we establish that Atg11 contributes to genome stability by performing a critical role in spindle positioning which is autophagy-independent in *S. cerevisiae.*

The plus and minus-end-directed molecular motors function either in concert or antagonistically to regulate the dynamics of microtubules. Kip2, a plus-end-directed motor, antagonizes the function of minus-end-directed motors like Kar3, Dyn1, and Kip3 in regulating the length of cytoplasmic microtubules and contributes to the spindle positioning (Cottingham and Hoyt, 1997). In this study, we show unanticipated and novel genetic interactions between Atg11 with these proteins. Atg11 displayed positive genetic interactions with MT plus-end proteins and negative with minus-end proteins hinting that Atg11 likely has a role at the SPBs in spindle positioning. Budding yeast engages Kar9 at metaphase, and Dyn1 at anaphase, to position the mitotic spindle along the mother-bud axis. Cells deficient of either Kar9 or Dyn1 display spindle misorientation, with anaphase nuclear division occurring in the mother cell, while cells lacking both are inviable (Li et al., 1993, Miller and Rose, 1998). Some of the proteins which contribute to spindle positioning in the Kar9 pathway include Nud1, an SPB component, mitotic exit network (MEN) proteins (Tem1, Cdc15, Dbf2-Dbf20), and ubiquitin-protein ligases, Dma1 and Dma2 (Fraschini et al., 2004, Hotz et al., 2012). Cellular fitness and binucleate cell phenotype of *atg11*Δ *dyn1*Δ and *atg11*Δ *kar9*Δ double mutants suggested that Atg11 functions in the Kar9 pathway and adds to the existing list of proteins important for spindle positioning. The *atg11*Δ *dyn1*Δ double mutant showing an increased proportion of binucleated cells along with a bypass of mitotic exit is in line with those observed upon deletion of *KIN4* or *DMA1 DMA2* in the *dyn1*Δ mutant background (D'Aquino et al., 2005, Fraschini et al., 2004). Thus, Atg11, similar to Kin4, Dma1 and Dma2, prevents mitotic exit in the absence of dynein.

Cell cycle-dependent kinases and phosphatases ensure the asymmetric distribution of proteins on the two SPBs and facilitate the asymmetric inheritance of SPBs during the cell cycle (Bardin et al., 2000, Manzano-Lopez et al., 2019, Miller and Rose, 1998, Molk et al., 2004). Atg11 localizing close to the old SPB during the metaphase-anaphase transition adds to the list of proteins localizing differentially to the dSPB. Physical association between Atg11-Spc72 and the loss of Spc72 asymmetry upon *ATG11* deletion demonstrated in this study uncovers the role of Atg11 in mediating Spc72 asymmetry (Figure 5A). We posit that Atg11 could function as an adaptor protein for Spc72. Alternatively, Atg11 can indirectly help other regulators in the asymmetric Kar9 establishment to the dSPB. Cdc5, a polo-like kinase, physically interacts with Spc72 at dSPB during the metaphase-anaphase transition and facilitates the asymmetric localization of Kar9 (Matellan et al., 2020), which in turn regulates asymmetric SPB inheritance (Matellan et al., 2020, Moore et al., 2006, Pereira et al., 2001). Loss of either Nud1, MEN components or Spc72 results in SPB inheritance defects along with

a loss in cell viability at an elevated temperature (Hotz et al., 2012, Matellan et al., 2020, Soues and Adams, 1998). Remarkably, the *atg11*Δ cells displayed similar defects, which strongly suggest that Atg11 plays a role in spindle positioning that is dependent on Kar9 and shares the function of preventing mitotic exit in the presence of spindle mispositioning (Figure 5B). How Atg11 prevents mitotic exit in cells with a mispositioned spindle remains to be investigated. Overexpression of Atg11, like Dma1 overexpression (Fraschini et al., 2004), rescuing the checkpoint defects of cells lacking Bub2 and preventing the cells from re-replicating their DNA will shed light on the role of Atg11 in mitotic exit.

While both mitosis and autophagy are evolutionarily conserved processes, the former is required for active growth in nutrient-rich media while the latter is critical under nutrient starvation. Our findings are significant in the light of the emerging role of autophagy in genome stability in cells experiencing genotoxic stress and cell cycle regulation under starvation conditions (Matsui et al., 2013a, Vessoni et al., 2013). Atg11 mediating correct spindle alignment, revealed in this work, opens the possibility to understand further the molecular basis of crosstalk between Atg11, SPB inheritance, and SPOC in faithful chromosome segregation. This is important with increasing pieces of evidence establishing an interplay between errors in the spindle alignment with ageing and aneuploidy leading to the development of cancer and neurodegenerative diseases (Cheng et al., 2008, Knoblich, 2010, Lancaster and Knoblich, 2012, Manzano-Lopez et al., 2019, Yamashita et al., 2007).

Materials and Methods

Yeast strains, plasmids, and primers

All the strains used in this study are specified in supplementary table 1. Primer sequences and the plasmids used for strain construction are specified in supplementary table 2, and supplementary table 3 respectively.

Media and growth conditions

The yeast strains were grown on YEPD media (yeast extract 1%, peptone 2%, and dextrose 2%) at 30°C unless stated otherwise. For the growth assay in presence of thiabendazole (TBZ), overnight grown cultures of wild-type, autophagy mutants, *ctf19*Δ, *mcm16*Δ, and *ATG11* complemented strains were serially diluted and spotted on YEPD containing 50 µg mL^{-1} and imaged on 2 dpi or 36 h.

Interaction network

We first constructed a protein-protein interaction map by identifying the proteins which have been reported to either genetically or physically interact with each of the Atg proteins. We further extended the network to include the proteins that are known to interact with any of the primary interactor proteins. We gleaned these connections using Perl scripts to query the latest curation of the BioGRID yeast interactomes (Stark et al., 2006). To this end, only those protein-protein interactions were retained which were confirmed and corroborated across three or more independent studies.

To discern the biophysical underpinnings of Atg11-Spc72 interactions, we set out to perform a flexible protein-protein docking using a ClusPro-type algorithm (Kozakov et al., 2017) within the OptMAVEn-2.0 docking protocol (Chowdhury et al., 2018). The Atg11 structure does not have experimentally validated crystallographic coordinates – so we predicted the structure using a deep multiple sequence alignment and feeding it through the AlphaFold2 (AF2) pipeline (Jumper et al., 2021). The AF2-recommended MMSeq2 program (Steinegger and Soding, 2017) was first executed to obtain a deep multiple sequence alignment of the *Saccharomyces cerevisiae* Atg11 sequence against all known protein and metagenomic sequences (~270M sequences). The alignment was thus passed through the structure prediction module of AF2 to arrive at the PDB formatted atomic coordinates of Atg11. Docking of Atg11 with post-translationally modified hexapeptide Spc72 was performed using implicit solvation and the Rosetta force-field (*MinMover* module (Chaudhury et al., 2010)) to obtain energy-minimized complexes. From an ensemble of 100 possible binding conformations, the modal pose was chosen which exhibited the lowest static-structure binding enthalpy.

Construction of yeast strains

ATG11 deletion was carried out by one-step gene replacement (Gietz and Schiestl, 2007), having 40-bp homology region using HR34 and HR35 primer pairs having *HPH* marker providing resistance against hygromycin B amplified from pAG32. The deletion strain was confirmed by 5' and 3' junction primers (HR36 and HR37). *ATG11* deletion in F2351 strain (Manzano-Lopez et al., 2019), with Kar9-GFP and Spc72-mCherry tagged, was carried out using HR34 and HR35 primer pairs having *HPH* marker providing resistance against hygromycin B amplified from pAG32.

Double deletion mutants were obtained either by transforming the above *ATG11* deletion cassette in single deletion mutant background or by crossing a single deletion mutant in *a* mating background having G418 marker with *atg11*Δ cells in Mat*α* (BY4742) background having *HPH* selection. The diploid cells were sporulated and after digestion of the cell wall

and vortexing, the cells were plated first on YEPD with hygromycin. Growing colonies were patched on G418 and colonies growing on both the selection plates were mated again with both Mat*a* (BY4741) and Mat*α* (BY4742) to differentiate between haploid and diploid cells. Cells showing shmoo formation with only one mating type were taken forward for the assays.

For *atg11*Δ complementation, a ~3.9 kb fragment comprising the upstream and full-length sequence of *ATG11* was fused with a ~800 bp of *HIS3* fragment with its promoter having a 40-bp homology sequence of *ATG11* at its 3' end. The purified PCR product was transformed in the *atg11*Δ cells and the transformants were screened using HR116 and HR117 primers.

Construction of strain expressing GFP-Tub1 and H1-mCherry under its native promoter

To study the nuclear dynamics in wild-type and *atg11*Δ, we constructed a strain expressing H1-mCherry under its native promoter with mCherry tagged at the C-terminus of histone, H1 in a strain having tubulin tagged with GFP. The H1-mCherry tagging cassette was generated by overlap PCR. Briefly, the mCherry coding sequence was amplified from pAW8-mCherry having 44-bp homology at the 5' end of the primer (HR86) to the C-terminal of histone, H1 and 22-bp homology at the 3' end of the primer (HR87) to the N-terminal of leucine. Leucine ORF was amplified from pUG73 vector using HR88 (having 19-bp homology at the 5' end of the primer with C-terminal of mCherry) and HR89 (having 43-bp homology at the 3' end of the primer with downstream of histone, H1). Both the PCR products were mixed in equal molar ratio and full-length H1-mCherry cassette was amplified using HR90 and HR91 primer pairs. The strain expressing H1-mCherry was generated by transforming the tagging cassette by one-step gene replacement (Wach et al., 1994).

Construction of strain expressing GFP-Tub1 and Spc42-mCherry under its native promoter

To study the dynamics of microtubules, tubulin was tagged with GFP using the plasmid, pAFS125 (Straight et al., 1997). To visualize SPBs, Spc42, a component of the central plaque of SPB, was tagged with mCherry using the primers HR142 and HR143.

Construction of *MAD2* and *BUB2* deletion strain

MAD2 deletion was carried out by one-step gene replacement (Gietz and Schiestl, 2007), having 40-bp homology region using HR52 and HR53 primer pairs having *HPH* marker providing resistance against hygromycin B amplified from pAG32. The deletion strain was confirmed by 5' and 3' junction primers (HR66 and HR67). Similarly, *BUB2* deletion was

carried out having 40-bp homology region using HR202 and HR203 primer pairs having *HPH* marker providing resistance against hygromycin B amplified from pAG32. The deletion strain was confirmed by 5' and 3' junction primers (HR206 and HR207).

Stability of monocentric plasmid

The *atg1*Δ, *atg6*Δ, *atg11*Δ, *atg15*Δ, *atg17*Δ, *ctf19*Δ, and the isogenic wild-type strains were transformed with pRS313, a mono centromeric plasmid, and selected on a dropout media lacking histidine (SD-his). The transformants were then inoculated in a non-selective media, YEPD, and allowed to grow for 7-10 generations, followed by plating dilutions to obtain single colonies. The single colonies were subsequently patched onto SD-his (selective) and YEPD (non-selective) media. The mitotic stability was calculated by the number of colonies that were able to grow on selective media (SD-his) divided by the total number of colonies on non-selective media (YEPD).

Chromosome loss assay

The chromosome loss assay was performed in a strain harbouring an extra non-essential chromosome that carries *SUP11* that suppresses *ade2* mutation in the assay strain, YMH58a as previously described (Hieter et al., 1985). Cells retaining this extra chromosome grow as a white coloured colony, as the cells bypass *ade2* mutation. Loss of extra chromosome leads to the red-pigmented colony, similar to *ade2* mutant phenotype, implying loss of *SUP11* (Hieter et al., 1985). A single white colony of wild-type and *atg11*Δ cells were grown in non-selective media (YEPD) for 5-7 generations, both at 30°C and 37°C. The cells were plated on YEPD with 0.6 mg mL^{-1} adenine. The number of colonies showing chromosome loss at the first division was scored for each condition in three independent biological experiments.

Flow cytometry

For figure S3A, overnight grown cultures of wild-type and *atg11*Δ were inoculated to 0.1 OD_{600} and the samples were grown at 30°C and 37°C. The samples were collected at 0, 3, 6, 9, 12, and 24 h. For figures S5C and S5D, overnight grown cultures were set at 0.1 OD_{600} and were grown for 5 doublings at 30°C and 37°C. The cells were washed with RNase buffer (0.2 M Tris pH-7.5, 20 mM EDTA) and resuspended in 100 µL RNase buffer. The cells were treated with 10 µL of RNase A (10 mg mL^{-1}) overnight at 37°C. Cells were washed with 1x PBS and were finally resuspended in 400 µL 1x PBS and incubated overnight at 4°C. Cells were stained with propidium iodide (0.06 µg $µL^{-1}$) for 30 min in dark conditions, just before

the data acquisition. Data from 30, 000 singlet cells per transformants were collected using BD FACSAria^{TM} III and analyzed using FlowJo_V10 software. The experiments were repeated thrice using freshly streaked cultures and data represents mean ± standard error of mean (SEM) from three independent experiments and calculated using two-way ANOVA for multiple comparisons.

In vivo assay for kinetochore integrity: *CEN* transcriptional read-through assay

The *CEN* transcription read-through assay was done by using a reporter plasmid containing a *GAL1-10* promoter that initiates transcription of an actin-lacZ fusion gene. A wild-type centromere inserted in the actin intron inactivates the segregational function of the *CEN*. The transcriptional block created by the *CEN* DNA-protein complex is relaxed in putative kinetochore mutants which allows transcription read-through activity from the reporter plasmid. The reporter plasmid pAKD06+*CEN4* contains a β-galactosidase reporter gene with the selectable marker *URA3*. The construct is designed to direct the integration of the reporter via homologous recombination to the *ura3* locus on chromosome V of *S. cerevisiae.* The transformants were obtained on SD-ura media. The single colony was inoculated in 5 mL of synthetic media lacking uracil, containing 2% galactose and 0.3% raffinose and was grown to OD_{600}=1. The cell pellet was washed with water and resuspended in 1 mL of Z-buffer (60 mM Na_2HPO_4, 40 mM $NaH_2PO_4.2H_2O$, 10 mM KCl, 5 mM β-ME). 0.1 mL of this was taken for the determination of OD_{610}. 0.1 mL of Z-buffer was added to the remaining 0.9 mL of cells. The cells were then permeabilized by adding 50 µL of 0.1% SDS and 100 µL of chloroform (incubated at 30°C for 15 min). 0.2 mL of 4 mg mL^{-1} ONPG (ortho-nitrophenyl-β-galactoside) was added to the cell suspension and incubated at 30°C till yellow colour developed. The reaction was stopped by adding 0.5 mL of 1 M Na_2CO_3. Cells were spun down at 10,000 g and the clear supernatant was transferred to a fresh tube. The optical density of this solution was measured at 420 and 550 nm. The enzyme activity was normalized with respect to cell density. Units of β galactosidase were measured as:

$$\text{Miller units} = \frac{1000\,[(OD_{420})-1.75\times(OD_{550})]}{t \times v \times OD_{610}}$$

t= time of reaction (min)

v= volume of cell suspension used in the assay (mL)

Live-cell imaging

Wild-type and *atg11*Δ cells tagged with H1-mCherry (nucleus) and GFP-Tub1 (spindle) for nuclear segregation dynamics, or wild-type and *atg11*Δ cells tagged with Spc42-mCherry (SPB marker) and GFP-Tub1 (spindle) for SPB separation dynamics were grown overnight in YEPD medium and re-inoculated in YEPD at 0.2 OD_{600} for 3 h. The cells were pelleted at 3,000 g for 2 min. The cells were placed on a glass slide having a 2% agarose pad supplemented with 2% dextrose and the pad was sealed with a coverslip. Live-cell microscopy was performed using the Zeiss Axio Observer 7, equipped with Definite Focus. 2, Colibri 7 (LED source), TempController 2000-2 (PECON), a Plan-Apochromat 100x/1.40 oil DIC M27, EMCCD camera.

Live-cell imaging at 37°C was performed on an inverted confocal microscope (ZEISS, LSM880) equipped with a temperature-control chamber (Pecon incubator, XL multiSL), a Plan Apochromat 100x NA oil 1.4 objective and GaAsp photodetectors. For time-lapse microscopy, images were captured at a 5 min interval with 5% intensity exposure with 0.5 µm Z-steps using 488 nm and 587 nm for GFP and mCherry as excitation wavelength. All the images displayed were maximum intensity projection of images for each time using ImageJ.

Microscopic image acquisition and processing

Wild-type and deletion mutants tagged either with H1-mCherry (nucleus), or GFP-Tub1 (spindle), and Spc42-mCherry (SPB marker) were grown overnight in YEPD medium and re-inoculated in YEPD at 0.2 OD_{600} for 3 h. The cells were pelleted at 3,000 *g*. The cells were mounted on a glass slide having a 2% agarose pad supplemented with 2% dextrose and the pad was sealed with a coverslip. Large-budded (budding index of >0.6) cells of each strain were imaged using an inverted microscope (ZEISS, Axio Observer.Z1/7), a Plan-Apochromat 100x/1.40 oil DIC M27. The filters used were GFP/FITC 488, mCherry 561 for excitation, GFP/FITC 500/550 bandpass or GFP 495/500 and mCherry 565/650 or mCherry 580/750 bandpass for emission. Z-stacks at an interval of 0.5 µm were taken and maximum intensity projection for each image using ImageJ was projected.

For figures 4B, S4A-4B, S3B and S8D, cells were imaged using an inverted confocal microscope (ZEISS, LSM880) equipped with Airyscan module, 63x Plan Apochromat 1.4 NA. Z stacks were obtained at an interval of 1 µM, 488/516 and 561/595 nm excitation/emission wavelengths were used for GFP and mCherry respectively.

For figures 4E and S8E, the images were deconvoluted using the default programme with the ZEN Blue software (Zeiss).

Staining protocols

Vacuoles were visualized by staining with 7-amino-4-chloromethylcoumarin (CMAC) (ThermoFischer Scientific, Cat. No. C2110; CellTrackerTM Blue CMAC dye) dissolved in DMSO to give a 10 mM stock. Briefly, the cells were incubated with 10 μM dye at 30°C for 1 h 30 min. The cells were washed with 1× PBS thrice with 5 min incubation each and were imaged.

FM4-64 staining was performed to visualize the vacuolar membrane. Briefly, FM4-64 (ThermoFischer Scientific; Cat. No. T3166) was added at a concentration of 7.5 μM for 1 h. The cells were gently washed twice with 1x PBS and further incubated for 1 h in YEPD before microscopy.

Post-acquisition analysis

Spindle length was measured by tracking it using a straight line, and freehand (for bent spindle) tool in ImageJ after maximum intensity projection for each image. SPB to SPB distance was determined by measuring the distance between the centers of Spc42-mCherry fluorescence using a straight-line tool in ImageJ after maximum intensity projection for each image. Spindle orientation was measured on images that were maximum intensity projected using the angle tool in ImageJ. The angle was calculated by measuring the smaller of the two angles that the spindle forms intersecting the mother-bud axis of the cell. The budding index was represented as the ratio of the diameter of the daughter cell to the diameter of the mother cell. Throughout the manuscript, large-budded cells with a budding index of >0.6 are taken into consideration for all the analyses (Saunders et al., 1997). Statistical analyses were done using GraphPad Prism 8.4.0 software. Student's *t*-test followed by Unpaired *t*-test for comparing two groups. The data sets represented as bar graphs were analyzed using either One-way ANOVA or two-way ANOVA for multiple groups and have been mentioned in the figure legends where applicable. Scatter plots with data from three independent biological repeats were plotted as SuperPlots (Lord et al., 2020), displaying individual colour-coded data, along with independent means ± SEM, which were superimposed. The statistical analyses were done with three independent biological replicates.

Yeast two-hybrid assays

The full-length *ATG11* (~3534 bp), *SPC72* (~1869 bp), and *CNM67* (~1746 bp) were PCR amplified and cloned in frame with the Gal4 activation/ DNA binding domain in pGADC1 and pGBDC1 respectively at BamHI and SalI sites using oligos listed in supplementary file 2.

Yeast-two hybrid analyses were performed in the strain PJ69-4A as described previously (James et al., 1996). Briefly, bait and prey plasmids were co-transformed into the *S. cerevisiae* strain PJ69-4A. Positive interactions were scored by the appearance of white-coloured colonies on a synthetic defined medium containing 6 µg mL^{-1} adenine and by growth in presence of 2 mM 3-Amino-1,2,4-triazole (3-AT) (A8056, Sigma).

Competing Interests

The authors declare no competing interests.

Acknowledgements

We thank D. J. Klionsky, C. Kraft, S. K. Ghosh, S. Bhattacharyya, F. Monje-Casas for sharing yeast strains and vectors, and G. Dey for the valuable comments. We thank N. Nala for his assistance with flow cytometry and B. Suma and K. Jayaram at the imaging facility at JNCASR. Financial support from the DBT-RA Program in Biotechnology and Life Sciences is gratefully acknowledged by MHR. The award of JC Bose Fellowship (JCB/2020/000021), SERB, and JNCASR intramural funding support to KS is acknowledged. This work was also supported by the Department of Biotechnology (DBT) grant in Life Science Research, Education and Training at JNCASR (BT/INF/22/SP27679/2018) and SERB grant (CRG/2019/004892) to RM. JV was supported by intramural financial support from JNCASR. We also thank the members of Molecular Mycology Laboratory for their valuable inputs and comments. Some images were created with BioRender.com.

Author Contributions

K.S. conceived the idea; M.H.R. and K.S. designed experiments; M.H.R. performed the majority of the experiments; J.V. performed the initial screen of autophagy mutants involved in chromosome segregation; R.C. constructed the protein network and predicted protein structure. M.H.R., J.V., R.C., and R.M. contributed new reagents/analytical tools; M.H.R., J.V., and K.S. analyzed the data; M.H.R. and K.S. wrote the paper; K.S. gathered funding and supervised the work.

References

BARDIN, A. J., VISINTIN, R. & AMON, A. 2000. A mechanism for coupling exit from mitosis to partitioning of the nucleus. *Cell,* 102**,** 21-31.

BLOECHER, A., VENTURI, G. M. & TATCHELL, K. 2000. Anaphase spindle position is monitored by the *BUB2* checkpoint. *Nat Cell Biol,* 2**,** 556-8.

CHAUDHURY, S., LYSKOV, S. & GRAY, J. J. 2010. PyRosetta: a script-based interface for implementing molecular modeling algorithms using Rosetta. *Bioinformatics,* 26**,** 689-91.

CHENG, J., TURKEL, N., HEMATI, N., FULLER, M. T., HUNT, A. J. & YAMASHITA, Y. M. 2008. Centrosome misorientation reduces stem cell division during ageing. *Nature,* 456**,** 599-604.

CHOWDHURY, R., ALLAN, M. F. & MARANAS, C. D. 2018. OptMAVEn-2.0: De novo design of variable antibody regions against targeted antigen epitopes. *Antibodies,* 7**,** 23.

COTTINGHAM, F. R. & HOYT, M. A. 1997. Mitotic spindle positioning in *Saccharomyces cerevisiae* is accomplished by antagonistically acting microtubule motor proteins. *J Cell Biol,* 138**,** 1041-53.

D'AQUINO, K. E., MONJE-CASAS, F., PAULSON, J., REISER, V., CHARLES, G. M., LAI, L., SHOKAT, K. M. & AMON, A. 2005. The protein kinase Kin4 inhibits exit from mitosis in response to spindle position defects. *Mol Cell,* 19**,** 223-34.

DOTIWALA, F., EAPEN, V. V., HARRISON, J. C., ARBEL-EDEN, A., RANADE, V., YOSHIDA, S. & HABER, J. E. 2013. DNA damage checkpoint triggers autophagy to regulate the initiation of anaphase. *Proc Natl Acad Sci U S A,* 110**,** E41-9.

FARACHE, D., EMORINE, L., HAREN, L. & MERDES, A. 2018. Assembly and regulation of gamma-tubulin complexes. *Open Biol,* 8.

FRASCHINI, R., BILOTTA, D., LUCCHINI, G. & PIATTI, S. 2004. Functional characterization of Dma1 and Dma2, the budding yeast homologues of *Schizosaccharomyces pombe* Dma1 and human Chfr. *Mol Biol Cell,* 15**,** 3796-810.

GEISSLER, S., PEREIRA, G., SPANG, A., KNOP, M., SOUES, S., KILMARTIN, J. & SCHIEBEL, E. 1996. The spindle pole body component Spc98p interacts with the gamma-tubulin-like Tub4p of *Saccharomyces cerevisiae* at the sites of microtubule attachment. *EMBO J,* 15**,** 3899-911.

GEYMONAT, M., PENG, Q., GUO, Z., YU, Z., UNRUH, J. R., JASPERSEN, S. L. & SEGAL, M. 2020. Orderly assembly underpinning built-in asymmetry in the yeast centrosome duplication cycle requires cyclin-dependent kinase. *Elife,* 9.

GIETZ, R. D. & SCHIESTL, R. H. 2007. High-efficiency yeast transformation using the LiAc/SS carrier DNA/PEG method. *Nature Protoc,* 2**,** 31.

GRUNEBERG, U., CAMPBELL, K., SIMPSON, C., GRINDLAY, J. & SCHIEBEL, E. 2000. Nud1p links astral microtubule organization and the control of exit from mitosis. *EMBO J,* 19**,** 6475-88.

HIETER, P., MANN, C., SNYDER, M. & DAVIS, R. W. 1985. Mitotic stability of yeast chromosomes: a colony color assay that measures nondisjunction and chromosome loss. *Cell,* 40**,** 381-92.

HOTZ, M., LEISNER, C., CHEN, D., MANATSCHAL, C., WEGLEITER, T., OUELLET, J., LINDSTROM, D., GOTTSCHLING, D. E., VOGEL, J. & BARRAL, Y. 2012. Spindle pole bodies exploit the mitotic exit network in metaphase to drive their age-dependent segregation. *Cell,* 148**,** 958-72.

HUYETT, A., KAHANA, J., SILVER, P., ZENG, X. & SAUNDERS, W. S. 1998. The Kar3p and Kip2p motors function antagonistically at the spindle poles to influence cytoplasmic microtubule numbers. *J Cell Sci,* 111**,** 295-301.

JAMES, P., HALLADAY, J. & CRAIG, E. A. 1996. Genomic libraries and a host strain designed for highly efficient two-hybrid selection in yeast. *Genetics,* 144**,** 1425-36.

JUANES, M. A., TWYMAN, H., TUNNACLIFFE, E., GUO, Z., TEN HOOPEN, R. & SEGAL, M. 2013. Spindle pole body history intrinsically links pole identity with asymmetric fate in budding yeast. *Curr Biol,* 23**,** 1310-9.

JUMPER, J., EVANS, R., PRITZEL, A., GREEN, T., FIGURNOV, M., RONNEBERGER, O., TUNYASUVUNAKOOL, K., BATES, R., ZIDEK, A., POTAPENKO, A., BRIDGLAND, A., MEYER, C., KOHL, S. A. A., BALLARD, A. J., COWIE, A., ROMERA-PAREDES, B., NIKOLOV, S., JAIN, R.,

660 ADLER, J., BACK, T., PETERSEN, S., REIMAN, D., CLANCY, E., ZIELINSKI, M., STEINEGGER, M.,
661 PACHOLSKA, M., BERGHAMMER, T., BODENSTEIN, S., SILVER, D., VINYALS, O., SENIOR, A. W.,
662 KAVUKCUOGLU, K., KOHLI, P. & HASSABIS, D. 2021. Highly accurate protein structure
663 prediction with AlphaFold. *Nature,* 596**,** 583-589.
664 KNOBLICH, J. A. 2010. Asymmetric cell division: recent developments and their implications for
665 tumour biology. *Nat Rev Mol Cell Biol,* 11**,** 849-60.
666 KNOP, M., PEREIRA, G., GEISSLER, S., GREIN, K. & SCHIEBEL, E. 1997. The spindle pole body
667 component Spc97p interacts with the gamma-tubulin of *Saccharomyces cerevisiae* and
668 functions in microtubule organization and spindle pole body duplication. *EMBO J,* 16**,** 1550-
669 64.
670 KNOP, M. & SCHIEBEL, E. 1997. Spc98p and Spc97p of the yeast gamma-tubulin complex mediate
671 binding to the spindle pole body via their interaction with Spc110p. *EMBO J,* 16**,** 6985-95.
672 KNOP, M. & SCHIEBEL, E. 1998. Receptors determine the cellular localization of a gamma-tubulin
673 complex and thereby the site of microtubule formation. *EMBO J,* 17**,** 3952-67.
674 KOLLMAN, J. M., MERDES, A., MOUREY, L. & AGARD, D. A. 2011. Microtubule nucleation by gamma-
675 tubulin complexes. *Nat Rev Mol Cell Biol,* 12**,** 709-21.
676 KORINEK, W. S., COPELAND, M. J., CHAUDHURI, A. & CHANT, J. 2000. Molecular linkage underlying
677 microtubule orientation toward cortical sites in yeast. *Science,* 287**,** 2257-9.
678 KOZAKOV, D., HALL, D. R., XIA, B., PORTER, K. A., PADHORNY, D., YUEH, C., BEGLOV, D. & VAJDA, S.
679 2017. The ClusPro web server for protein-protein docking. *Nat Protoc,* 12**,** 255-278.
680 LANCASTER, M. A. & KNOBLICH, J. A. 2012. Spindle orientation in mammalian cerebral cortical
681 development. *Curr Opin Neurobiol,* 22**,** 737-46.
682 LEE, L., TIRNAUER, J. S., LI, J., SCHUYLER, S. C., LIU, J. Y. & PELLMAN, D. 2000. Positioning of the
683 mitotic spindle by a cortical-microtubule capture mechanism. *Science,* 287**,** 2260-2.
684 LENGEFELD, J. & BARRAL, Y. 2018. Asymmetric segregation of aged spindle pole bodies during cell
685 division: Mechanisms and relevance beyond budding yeast? *Bioessays,* 40**,** e1800038.
686 LI, Y. Y., YEH, E., HAYS, T. & BLOOM, K. 1993. Disruption of mitotic spindle orientation in a yeast
687 dynein mutant. *Proc Natl Acad Sci U S A,* 90**,** 10096-100.
688 LIAKOPOULOS, D., KUSCH, J., GRAVA, S., VOGEL, J. & BARRAL, Y. 2003. Asymmetric loading of Kar9
689 onto spindle poles and microtubules ensures proper spindle alignment. *Cell,* 112**,** 561-74.
690 LIN, T. C., NEUNER, A. & SCHIEBEL, E. 2015. Targeting of gamma-tubulin complexes to microtubule
691 organizing centers: conservation and divergence. *Trends Cell Biol,* 25**,** 296-307.
692 LORD, S. J., VELLE, K. B., MULLINS, R. D. & FRITZ-LAYLIN, L. K. 2020. SuperPlots: Communicating
693 reproducibility and variability in cell biology. *Journal of Cell Biology,* 219.
694 MANZANO-LOPEZ, J., MATELLAN, L., ALVAREZ-LLAMAS, A., BLANCO-MIRA, J. C. & MONJE-CASAS, F.
695 2019. Asymmetric inheritance of spindle microtubule-organizing centres preserves
696 replicative lifespan. *Nat Cell Biol,* 21**,** 952-965.
697 MATELLAN, L., MANZANO-LOPEZ, J. & MONJE-CASAS, F. 2020. Polo-like kinase acts as a molecular
698 timer that safeguards the asymmetric fate of spindle microtubule-organizing centers. *Elife,* 9.
699 MATSCHEKO, N., MAYRHOFER, P., RAO, Y., BEIER, V. & WOLLERT, T. 2019. Atg11 tethers Atg9
700 vesicles to initiate selective autophagy. *PLoS Biol,* 17**,** e3000377.
701 MATSUI, A., KAMADA, Y. & MATSUURA, A. 2013a. The role of autophagy in genome stability through
702 suppression of abnormal mitosis under starvation. *PLoS genetics,* 9**,** e1003245-e1003245.
703 MATSUI, A., KAMADA, Y. & MATSUURA, A. 2013b. The role of autophagy in genome stability through
704 suppression of abnormal mitosis under starvation. *PLoS Genet,* 9**,** e1003245.
705 MEZIANE, M., GENTHIAL, R. & VOGEL, J. 2021. Kar9 symmetry breaking alone is insufficient to ensure
706 spindle alignment. *Sci Rep,* 11**,** 4227.
707 MILLER, R. K., CHENG, S. C. & ROSE, M. D. 2000. Bim1p/Yeb1p mediates the Kar9p-dependent
708 cortical attachment of cytoplasmic microtubules. *Mol Biol Cell,* 11**,** 2949-59.
709 MILLER, R. K. & ROSE, M. D. 1998. Kar9p is a novel cortical protein required for cytoplasmic
710 microtubule orientation in yeast. *J Cell Biol,* 140**,** 377-90.

711 MOLK, J. N., SCHUYLER, S. C., LIU, J. Y., EVANS, J. G., SALMON, E. D., PELLMAN, D. & BLOOM, K. 2004.
712 The differential roles of budding yeast Tem1p, Cdc15p, and Bub2p protein dynamics in
713 mitotic exit. *Mol Biol Cell,* 15**,** 1519-32.
714 MOORE, J. K., D'SILVA, S. & MILLER, R. K. 2006. The CLIP-170 homologue Bik1p promotes the
715 phosphorylation and asymmetric localization of Kar9p. *Mol Biol Cell,* 17**,** 178-91.
716 NELSON, S. A., SANSON, A. M., PARK, H. O. & COOPER, J. A. 2012. A novel role for the GTPase-
717 activating protein Bud2 in the spindle position checkpoint. *PLoS One,* 7**,** e36127.
718 NIEDERSTRASSER, H., SALEHI-HAD, H., GAN, E. C., WALCZAK, C. & NOGALES, E. 2002. XKCM1 acts on
719 a single protofilament and requires the C terminus of tubulin. *J Mol Biol,* 316**,** 817-28.
720 PEREIRA, G., GRUENEBERG, U., KNOP, M. & SCHIEBEL, E. 1999. Interaction of the yeast gamma-
721 tubulin complex-binding protein Spc72p with Kar1p is essential for microtubule function
722 during karyogamy. *EMBO J,* 18**,** 4180-95.
723 PEREIRA, G., HOFKEN, T., GRINDLAY, J., MANSON, C. & SCHIEBEL, E. 2000. The Bub2p spindle
724 checkpoint links nuclear migration with mitotic exit. *Mol Cell,* 6**,** 1-10.
725 PEREIRA, G., TANAKA, T. U., NASMYTH, K. & SCHIEBEL, E. 2001. Modes of spindle pole body
726 inheritance and segregation of the Bfa1p-Bub2p checkpoint protein complex. *EMBO J,* 20**,**
727 6359-70.
728 SAUNDERS, W., HORNACK, D., LENGYEL, V. & DENG, C. 1997. The *Saccharomyces cerevisiae* kinesin-
729 related motor Kar3p acts at preanaphase spindle poles to limit the number and length of
730 cytoplasmic microtubules. *J Cell Biol,* 137**,** 417-31.
731 SEGAL, M. & BLOOM, K. 2001. Control of spindle polarity and orientation in *Saccharomyces*
732 *cerevisiae*. *Trends Cell Biol,* 11**,** 160-6.
733 SOUES, S. & ADAMS, I. R. 1998. *SPC72*: a spindle pole component required for spindle orientation in
734 the yeast *Saccharomyces cerevisiae*. *J Cell Sci,* 111 (Pt 18)**,** 2809-18.
735 STARK, C., BREITKREUTZ, B. J., REGULY, T., BOUCHER, L., BREITKREUTZ, A. & TYERS, M. 2006.
736 BioGRID: a general repository for interaction datasets. *Nucleic Acids Res,* 34**,** D535-9.
737 STEINEGGER, M. & SODING, J. 2017. MMseqs2 enables sensitive protein sequence searching for the
738 analysis of massive data sets. *Nat Biotechnol,* 35**,** 1026-1028.
739 STRAIGHT, A. F., MARSHALL, W. F., SEDAT, J. W. & MURRAY, A. W. 1997. Mitosis in living budding
740 yeast: anaphase A but no metaphase plate. *Science,* 277**,** 574-8.
741 STROME, E. D., WU, X., KIMMEL, M. & PLON, S. E. 2008. Heterozygous screen in *Saccharomyces*
742 *cerevisiae* identifies dosage-sensitive genes that affect chromosome stability. *Genetics,* 178**,**
743 1193-1207.
744 VESSONI, A. T., FILIPPI-CHIELA, E. C., MENCK, C. F. & LENZ, G. 2013. Autophagy and genomic
745 integrity. *Cell Death Differ,* 20**,** 1444-54.
746 WACH, A., BRACHAT, A., POHLMANN, R. & PHILIPPSEN, P. 1994. New heterologous modules for
747 classical or PCR-based gene disruptions in *Saccharomyces cerevisiae*. *Yeast,* 10**,** 1793-808.
748 WANG, Y., HU, F. & ELLEDGE, S. J. 2000. The Bfa1/Bub2 GAP complex comprises a universal
749 checkpoint required to prevent mitotic exit. *Curr Biol,* 10**,** 1379-82.
750 WANG, Y., ZHANG, X., ZHANG, H., LU, Y., HUANG, H., DONG, X., CHEN, J., DONG, J., YANG, X., HANG,
751 H. & JIANG, T. 2012. Coiled-coil networking shapes cell molecular machinery. *Mol Biol Cell,*
752 23**,** 3911-22.
753 WINEY, M. & BLOOM, K. 2012. Mitotic spindle form and function. *Genetics,* 190**,** 1197-224.
754 YAMASHITA, Y. M., MAHOWALD, A. P., PERLIN, J. R. & FULLER, M. T. 2007. Asymmetric inheritance of
755 mother versus daughter centrosome in stem cell division. *Science,* 315**,** 518-21.
756 YEH, E., SKIBBENS, R. V., CHENG, J. W., SALMON, E. D. & BLOOM, K. 1995. Spindle dynamics and cell
757 cycle regulation of dynein in the budding yeast, *Saccharomyces cerevisiae*. *J Cell Biol,* 130**,**
758 687-700.
759 YIN, H., PRUYNE, D., HUFFAKER, T. C. & BRETSCHER, A. 2000. Myosin V orientates the mitotic spindle
760 in yeast. *Nature,* 406**,** 1013-5.

761

Figures and figure legends

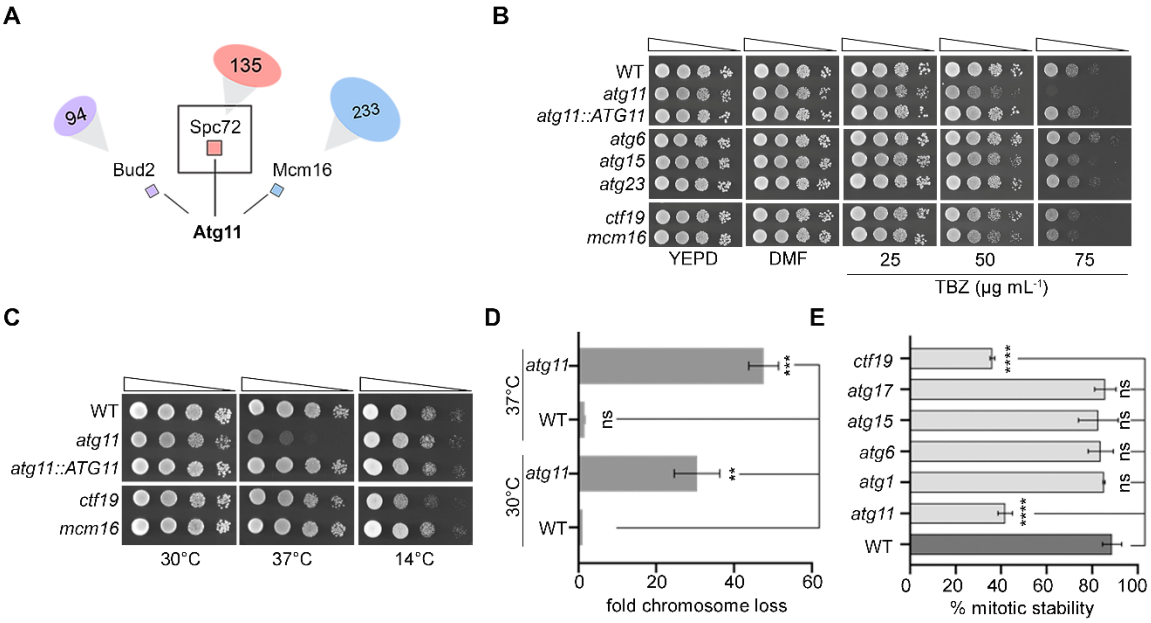

Figure 1. Cells lacking Atg11 display an increased rate of chromosome loss. (A) Primary (square boxes) and secondary (oval) interactors of Atg11 as reported in the latest curation of BioGRID (Stark et al., 2006). (B) Exponentially growing cells of wild-type (WT), various autophagy mutants such as *atg11*Δ, *atg11*Δ*::ATG11*, *atg6*Δ, *atg15*Δ, *atg23*Δ, and kinetochore mutant strains *ctf19*Δ, and *mcm16*Δ were 10-fold serially diluted and spotted on YEPD, and YEPD plates containing dimethylformamide (DMF, solvent control) or increasing concentration of thiabendazole (TBZ) as indicated. Plates were photographed after incubation for 2 days at 30°C. (C) Exponentially growing cells of indicated strains were 10-fold serially diluted and spotted on YEPD plates. Plates were photographed after 2 days of incubation, but 7 days post-inoculation (dpi) for 14°C. (D) Bar graph showing fold increase in chromosome loss in wild-type and *atg11*Δ strains at 30°C and 37°C. Error bar indicates standard deviation (SD), and statistical analysis was done using one-way ANOVA at $p<0.05$. (E) Mitotic stability of a monocentric plasmid (pRS313) was determined in wild-type, autophagy mutants as indicated and, in the kinetochore, mutant strain *ctf19*Δ. The assay was done with three independent sets of transformants. Statistical analysis was done using one-way ANOVA (****$p<0.0001$).

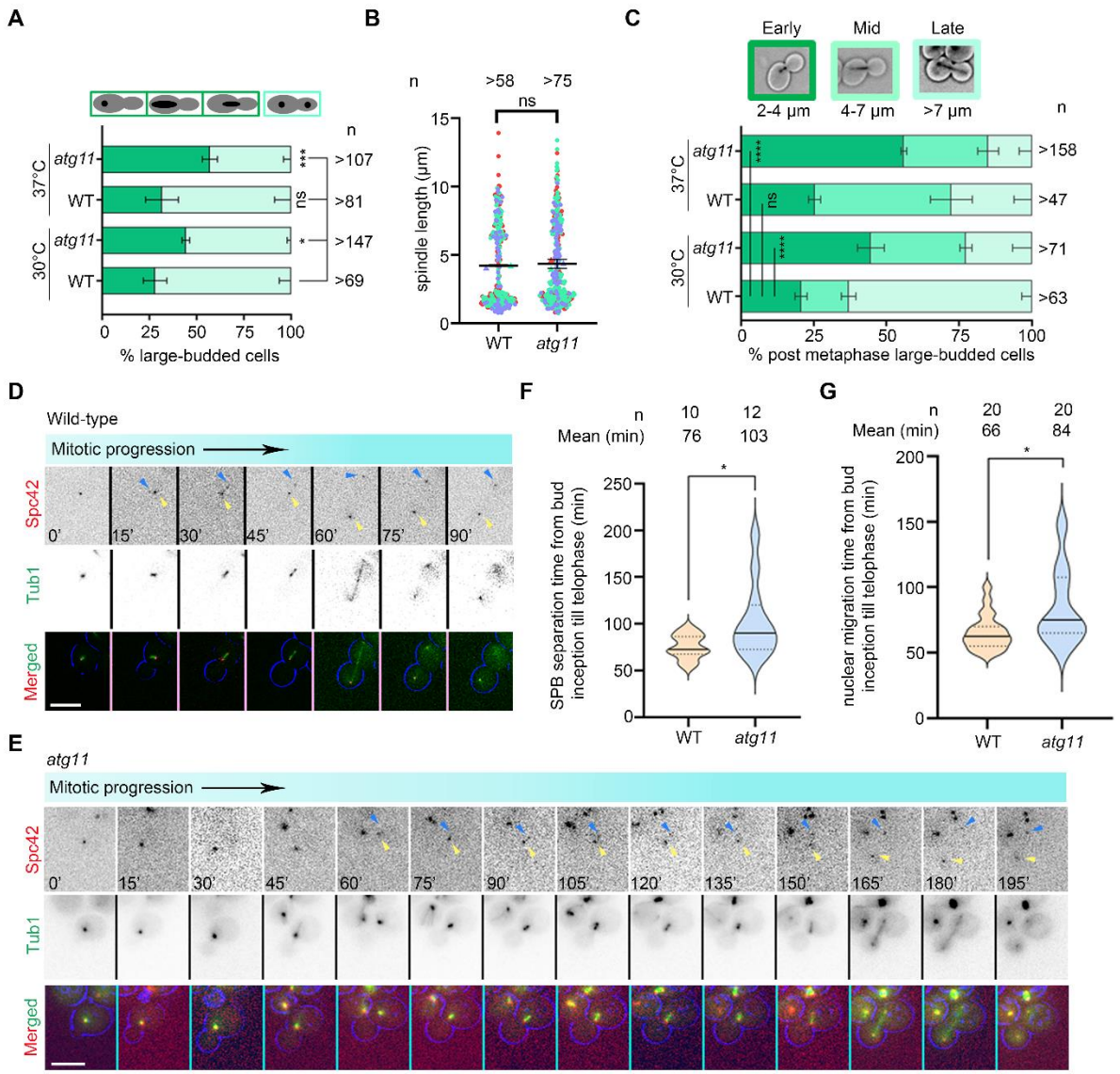

Figure 2. The *atg11*Δ cells show a delayed entry into anaphase. (A) Bar graph representing the percent large-budded cells (budding index >0.6) having the nucleus either segregated (light green) or unsegregated (dark green) in wild-type (WT) and *atg11*Δ cells at the indicated temperatures. Error bars show mean ± standard deviation (SD) from three biological replicates. Cartoons represent cellular morphology (grey), and chromatin mass (black) associated with the corresponding class. n represents the minimum number of large-budded cells analyzed in three independent biological replicates. Wild-type, n= 69-101 and 81-160 grown at 30°C and 37°C respectively. *atg11*Δ, n= 147-168 and 107-135 grown at 30°C and 37°C respectively. Statistical analysis was done using two-way ANOVA for multiple comparisons (*p<0.0182 and ***p<0.0001). (B) A scatter plot displaying the spindle (GFP-Tub1) length in wild-type and *atg11*Δ strains. Data represent mean ± standard error of mean (SEM) from three independent experiments and calculated using unpaired *t*-test at p<0.05. n represents the minimum number

of cells analyzed in three independent biological replicates. Wild-type, n= 58-129 and *atg11*Δ, n= 75-164. (C) A bar graph representing the percent post-metaphase large-budded cells having early (2-4 μm), mid (4-7 μm), and late (>7 μm) anaphase spindle (GFP-Tub1) in wild-type and *atg11*Δ cells at 30°C and 37°C. n represents the minimum number of large-budded cells (budding index of >0.6) analyzed in three independent biological replicates. Wild-type, n= 63-73 and 47-80 grown at 30°C and 37°C respectively. *atg11*Δ, n= 71-125 and 58-135 grown at 30°C and 37°C respectively. Error bars show mean ± SEM. Statistical analysis was done using two-way ANOVA for multiple comparisons at $p<0.05$. (D-E) A representative montage of the time-lapse image showing SPB (Spc42-mCherry) separation and spindle (GFP-Tub1) elongation dynamics in wild-type and *atg11*Δ cells respectively at 30°C. Based on fluorescence signal intensities, old and new SPBs are marked by yellow and blue arrowheads, respectively. Scale bar, 5 μm. (F) A violin plot displaying the time taken for the completion of SPB separation between mother and daughter cells during the cell cycle from the inception of bud in strains as indicated. The number on top represents the average time taken for the completion of SPB separation. The continuous black line on the violin plot represents the median, while the dotted lines represent quartiles. The statistical significance was done using an unpaired *t*-test with Welch's correction at $p<0.0398$. (G) A violin plot displaying the time taken for the segregation of the nucleus in the two cells during the cell cycle from the bud inception in strains as indicated. The number on top represents the average time taken for the completion of nuclear migration. The statistical significance was done using an unpaired *t*-test with Welch's correction at $p<0.0142$.

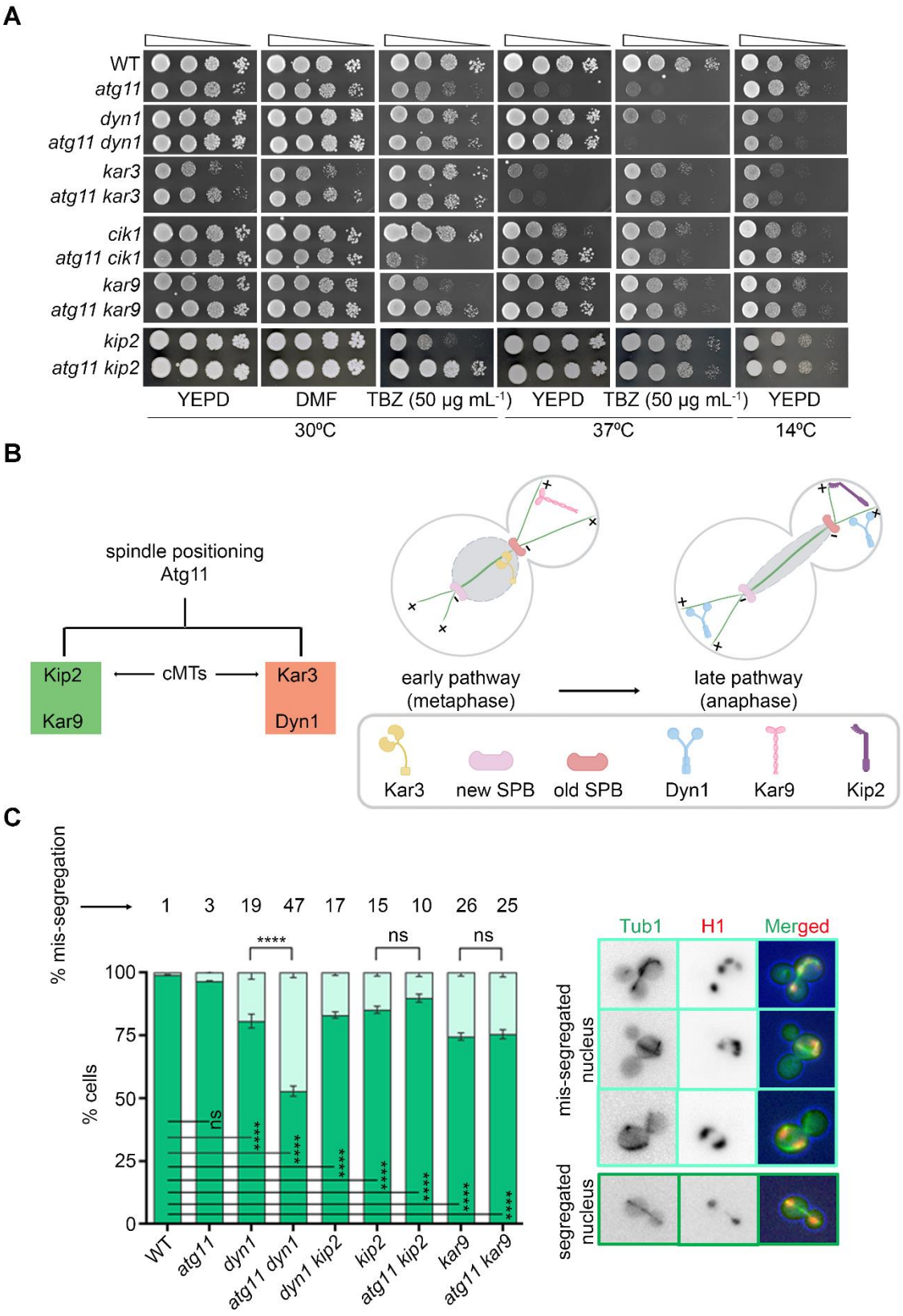

Figure 3. Atg11 is required for proper spatiotemporal positioning of the mitotic spindle. (A) Growth of wild-type *atg11*Δ strains, and null mutants of kinesin-related motors and Atg11-interacting proteins at the indicated temperature and in presence of the microtubule poison

TBZ. The cells were 10-fold serially diluted and spotted on YEPD, and YEPD containing TBZ. DMF was used as a no-drug control. Plates were photographed after 2 days of incubation, but 7 days post-inoculation (dpi) for 14°C. (B) Schematic summarizing novel positive (green) and negative (red) genetic interactions observed between Atg11 and regulators of mitotic spindle positioning. Kip2 and Kar3 regulate the length of cytoplasmic microtubules (cMTs), while Kar9 and Dyn1 regulate spindle positioning in metaphase, in the early pathway, and anaphase, in the late pathway, respectively. (C) Bar graph showing the percent cells with segregated (dark green) nuclei in the mother and daughter cells, and mis-segregated (light green) binucleated and multinucleated nuclei. Error bars show mean ± standard error of mean (SEM). Statistical analysis was done using two-way ANOVA for multiple comparisons at $p<0.05$.

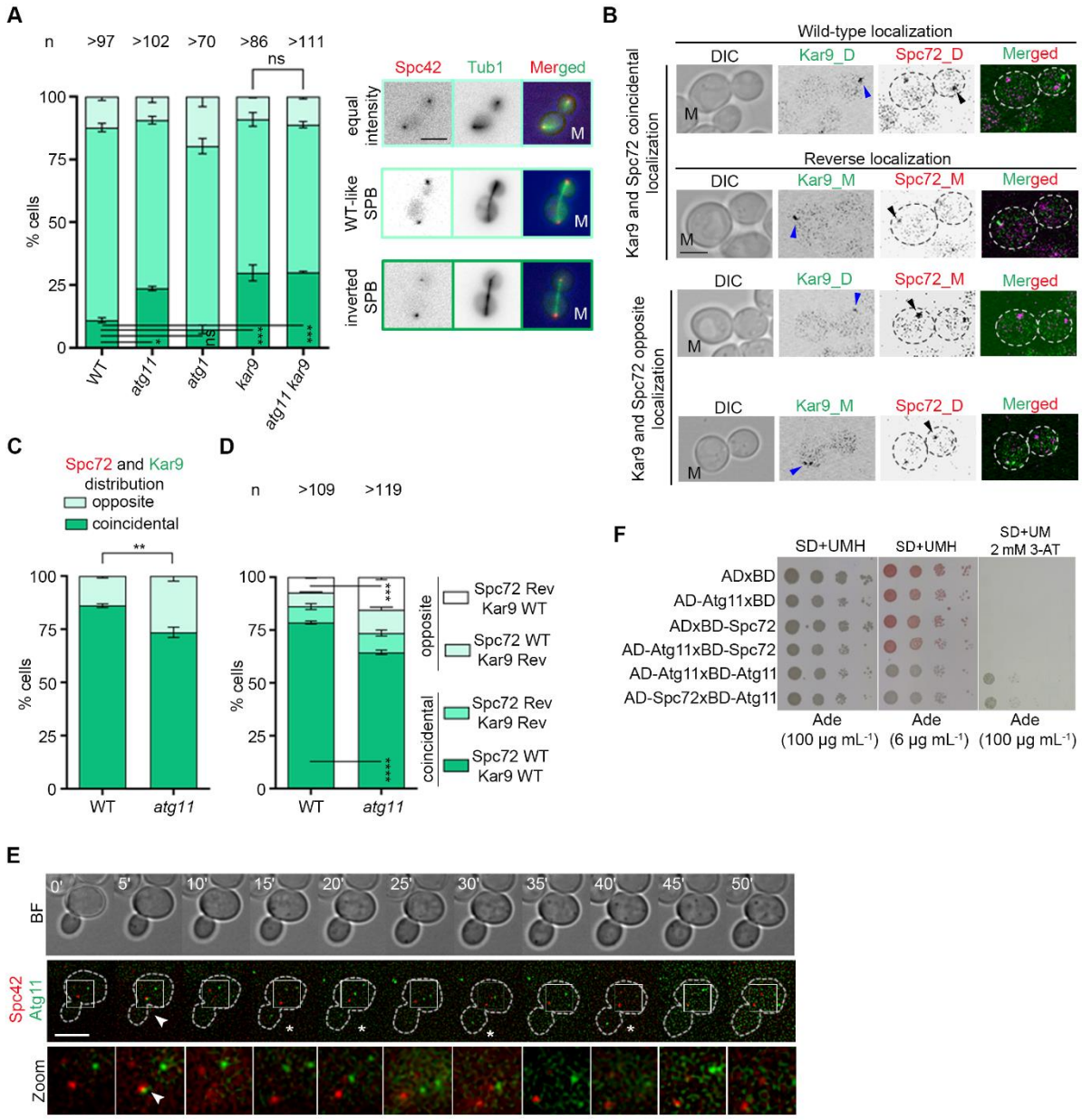

Figure 4. The *atg11*Δ cells exhibit inverted localization of Spc72 and Kar9 on the SPBs. (A) Bar graph displaying percent cells having wild-type-like (old SPB in the daughter cell), reversed (old SPB in the mother cell), or symmetric (SPBs are indistinguishable) SPB inheritance in the indicated strains based on the Spc42-mCherry signal intensity. *Right*, representative images of above mentioned SPB inheritance are shown. M represents the mother cell. The minimum number of cells analyzed from three independent biological replicates is mentioned as n. Wild-type, n= 97-167, *atg11*Δ, n= 102-154, *atg1*Δ, n= 70-87, *kar9*Δ, n= 86-145, and *atg11*Δ *kar9*Δ, n= 111-126. Statistical analysis was done using two-way ANOVA for multiple comparisons at $p<0.05$. Scale bar, 5 µm. (B) Representative images displaying coincidental or opposite distribution of Kar9-GFP (green) and Spc72-mCherry (magenta) in

wild-type and *atg11*Δ cells, exhibiting wild-type-like asymmetric and predominant accumulation of both the proteins in the bud or reversed such that asymmetric and predominant accumulation of these proteins in the mother (M) cell. Asymmetric localization of Kar9-GFP and Spc72-mCherry is marked by blue and black arrowheads respectively. Scale bar, 5 μm. (C, D) Bar graph representing the percent of cells displaying coincidental (dark green) and opposite (light green) Kar9-GFP and Spc72-mCherry localization (C). For coincidental and opposite Kar9-GFP and Spc72-mCherry localization, the wild-type and reversed distribution patterns are also further subclassified (D). The minimum number of cells analyzed is represented by n. Wild-type, n= 109-119, and *atg11*Δ, n= 119-122. Error bars show mean ± standard error of mean (SEM). Statistical analysis was done using two-way ANOVA at $p<0.05$. (E) Time-lapse images displaying the proximal localization of Atg11 with SPBs in wild-type cells having duplicated SPBs in mother cell. White arrowhead shows Atg11 being close first with the daughter SPB (dSPB) at 5 min. The asterisks show the dynamics of Atg11 localization in the daughter cell before the movement of daughter SPB (dSPB). Scale bar, 6 μm. (F) Yeast-two hybrid (Y2H) assay in *S. cerevisiae* strains carrying the mentioned plasmid combinations was 10-fold serially diluted and spotted on SD minimal medium plates lacking trypsin (trp) and leucine (leu) or trp, leu, and histidine (his) supplemented with 2 mM 3-amino-1,2,4-triazole (3-AT) and grown at 30°C.

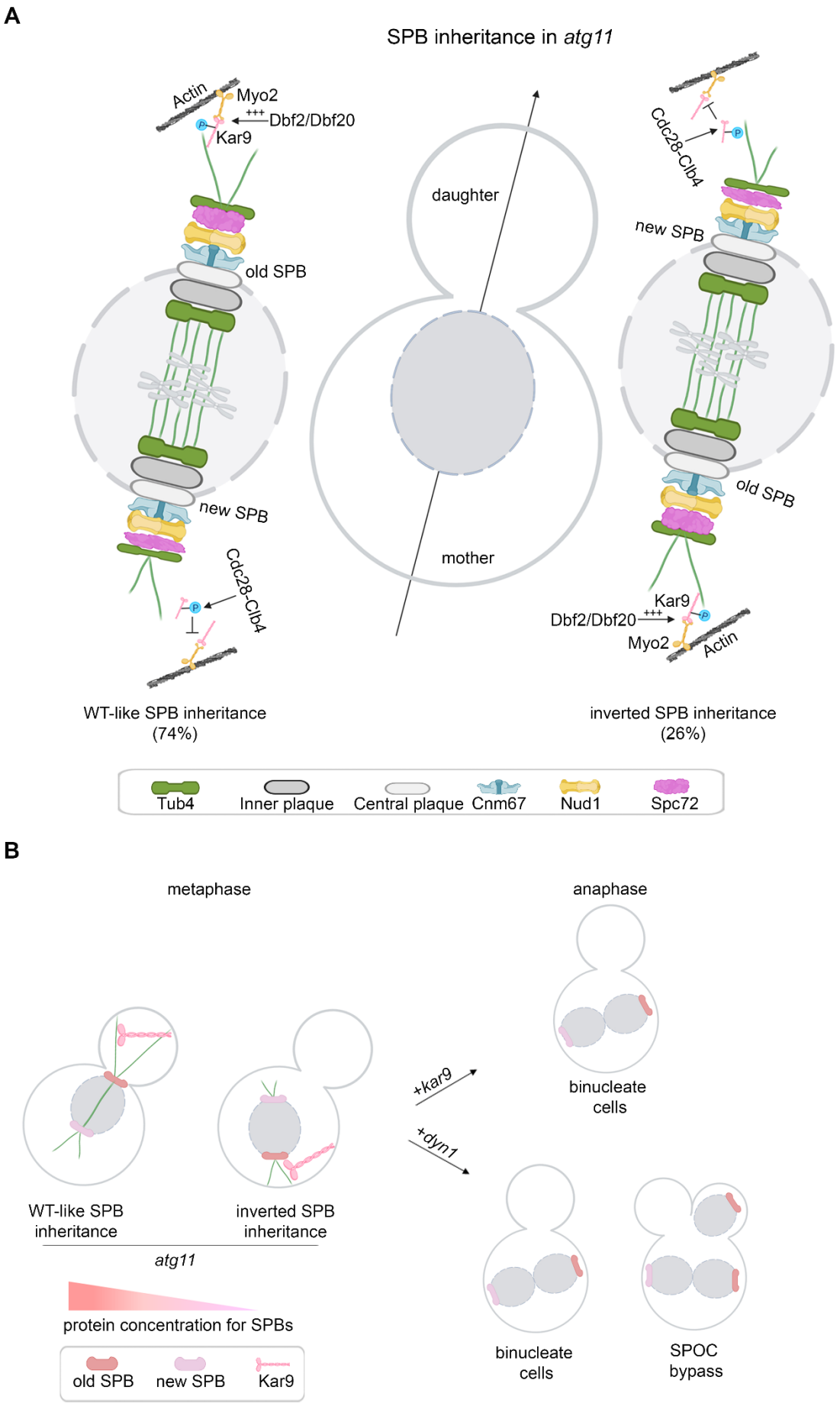
A
SPB inheritance in atg11
Actin
Myo2
+++
Dbf2/Dbf20
Kar9
old SPB
new SPB
Cdc28-Clb4
daughter
mother
Cdc28-Clb4
new SPB
old SPB
Kar9
Dbf2/Dbf20
+++
Myo2
Actin
WT-like SPB inheritance
(74%)
inverted SPB inheritance
(26%)
Tub4
Inner plaque
Central plaque
Cnm67
Nud1
Spc72
B
metaphase
anaphase
+kar9
+dyn1
binucleate cells
WT-like SPB inheritance
inverted SPB inheritance
atg11
protein concentration for SPBs
old SPB
new SPB
Kar9
binucleate cells
SPOC bypass

912

Figure 5. Atg11 mediates asymmetric SPB inheritance required for spindle alignment in *S. cerevisiae*. (A) Lack of Atg11 leads to the loss of Spc72 and Kar9 asymmetry, leading to SPB inheritance defects. (B) The *atg11*Δ cells display spindle mispositioning during metaphase and yield binucleate cells upon loss of Kar9, similar to defects associated with the *kar9*Δ cells. Loss of *ATG11* in the *dyn1*Δ cells results in a defect in the spindle position checkpoint, leading to the formation of multinucleated cells.